CrossMark

From γ to Radio: The Electromagnetic Counterpart of GW170817

Ehud Nakar[1], Ore Gottlieb[1], Tsvi Piran[2] [ID], Mansi. M. Kasliwal[3] [ID], and Gregg Hallinan[3]
[1] Raymond and Beverly Sackler School of Physics & Astronomy, Tel Aviv University, Tel Aviv 69978, Israel
[2] Racah Institute of Physics, The Hebrew University of Jerusalem, Jerusalem 91904, Israel
[3] Division of Physics, Math and Astronomy, California Institute of Technology, 1200 East California Boulevard, Pasadena, CA 91125, USA

Abstract

The gravitational waves from the first binary neutron star merger, GW170817, were accompanied by a multiwavelength electromagnetic counterpart, from γ-rays to radio. The accompanying γ-rays seem at first to confirm the association of mergers with short gamma-ray bursts (sGRBs). The common interpretation was that we see an emission from an sGRB jet seen off-axis. However, a closer examination of the subluminous γ-rays and the peculiar radio afterglow was inconsistent with this simple interpretation. Here we present results of 3D and 2D numerical simulations that follow the hydrodynamics and emission of the outflow from a neutron star merger, form its ejection and up to its deceleration by the circum-merger medium. Our results show that the current set of γ-rays, X-rays, and radio observations can be explained by the emission from a mildly relativistic cocoon material (Lorentz factor ∼2–5) that was formed while a jet propagated through the material ejected during the merger. The γ-rays are generated when the cocoon breaks out from the engulfing ejecta, while the afterglow is produced by interaction of the cocoon matter with the interstellar medium. The strong early UV/optical signal may be a Lorentz-boosted macronova/kilonova. The fate of the jet itself is currently unknown, but our full-electromagnetic (EM) models define a path to resolving between successful and choked jet scenarios, outputting coupled predictions for the image size, morphology, observed time-dependent polarization, and light-curve behavior from radio to X-ray. The predictive power of these models will prove key in interpreting the ongoing multifaceted observations of this unprecedented event.

Key words: gamma-ray burst: individual (GRB 170817A) – gravitational waves – stars: neutron

1. Introduction

At first glance GRB 170817A looks like a regular short gamma-ray burst (sGRB; Goldstein et al. 2017; Savchenko et al. 2017), thereby confirming the association of mergers with sGRBs (e.g., Eichler et al. 1989; Nakar 2007). However, a closer examination reveals that it does not resemble any other burst seen before. Its total isotropic equivalent luminosity is smaller by several orders of magnitude than the weakest short burst with an identified redshift. It is softer than typical sGRBs, and it has a unique spectral evolution: a harder ($E_p \sim 185 \pm 62\,\mathrm{keV}$) 0.6 s pulse, followed by a thermal tail ($kT \sim 10\,\mathrm{keV}$) lasting about 1 s. The observed afterglow was not less puzzling. A bright declining X-ray signal is observed in regular sGRBs from day 1. Here, only upper limits were obtained during the first week. The first X-ray detection (Margutti et al. 2017; Troja et al. 2017) was only at day 9. The first radio detection (Hallinan et al. 2017) was only at day 16.

The event was also accompanied by a UV/optical/IR signal detected 11 hr after the merger (e.g., Arcavi et al. 2017; Coulter et al. 2017; Covino et al. 2017; Díaz et al. 2017; McCully et al. 2017; Shappee et al. 2017; Soares-Santos et al. 2017; Utsumi et al. 2017; Buckley et al. 2018). The common macronova (a.k.a. kilonova) interpretation is that it was powered by radioactive decay within the dynamical ejecta and winds ejected during the merger (e.g., Cowperthwaite et al. 2017; Drout et al. 2017; Evans et al. 2017; Kasen et al. 2017; Kasliwal et al. 2017; Kilpatrick et al. 2017; Nicholl et al. 2017; Pian et al. 2017; Shappee et al. 2017; Smartt et al. 2017; Tanaka et al. 2017; Tanvir et al. 2017; Waxman et al. 2018). However, even this signal deviated somewhat from the expectations. It was too bright and too blue half a day after the merger. While clearly inconsistent with lanthanides high

opacity ($\kappa \approx 10\,\mathrm{cm^2\,g^{-1}}$), even a much lower opacity ($\kappa \approx 1\,\mathrm{cm^2\,g^{-1}}$) is hardly consistent with such a bright early signal (Kasliwal et al. 2017; Arcavi 2018).

The common explanation to the peculiar observations was that we have observed a regular sGRB jet off-axis (Goldstein et al. 2017; Haggard et al. 2017; Margutti et al. 2017; Troja et al. 2017). However, if that was the case, an observer that looked at the jet on-axis would have seen a very atypical sGRB (Granot et al. 2018; Kasliwal et al. 2017).[4] More importantly, the very strong dependence of the observed off-axis luminosity on the observing angle implies that in this interpretation the angle to the gamma-ray-emitting region must be small ($\lesssim 0.1$ rad; Kasliwal et al. 2017). Therefore a clear prediction of this model is a radio and X-ray afterglow that rises to a peak soon after the merger, which is inconsistent with the continuous rise seen during the first ∼100 days (Pooley et al. 2018; Lyman et al. 2018; Margutti et al. 2018; Mooley et al. 2018b; Ruan et al. 2018). Alternatively, the unique properties of the γ-rays suggest that we observed a mildly relativistic shock breakout. Compactness arguments show that the radiating material must have at least $\Gamma \approx 2$–3 (Gottlieb et al. 2018b), while the UV/optical/IR indicate that ∼0.05 $M_\odot$ were launched at velocities of 0.1c–0.3c during the merger. This suggests that a jet with $\Gamma \gtrsim 3$ was launched following the merger into the expanding ejecta. When the jet propagates through the subrelativistic ejecta, it inflates a cocoon (Ramirez-Ruiz et al. 2002). Nakar & Piran (2017), Lazzati et al. (2017a), and Gottlieb et al. (2018a) have shown before GW170817 that in the conditions expected following a neutron star merger the jet propagation gives rise to

---

[4] Simple Doppler arguments suggest that the peak photon energy of that burst would have been at least ≈5 MeV. Such a peak energy is much higher than the typically observed SGRB peak energy and is seen only rarely.

a wide-angle, mildly relativistic cocoon. Moreover, the cocoon is expected not only in cases in which the jet successfully breaks out of the subrelativistic ejecta, presumably producing a regular sGRB for an on-axis observer, but also in cases in which the jet is choked within the ejecta and no sGRB is generated.

Soon after the detection of GW170817, we and others suggested that the γ-rays were generated by the breakout of the shock driven by the cocoon out of the subrelativistic ejecta (Gottlieb et al. 2018b; Kasliwal et al. 2017; Bromberg et al. 2018; Pozanenko et al. 2018). The mildly relativistic shock breakout model is appealing since it explains all the properties of the signal: its low luminosity compared to the total explosion energy, its spectrum, its duration, and the delay compared to the GW signal. Moreover, the quasi-thermal spectrum and its hard-to-soft evolution are a clear prediction of shock breakout emission (Nakar & Sari 2012; Gottlieb et al. 2018b). In addition, all the unique properties of GRB 170817A are seen also in low-luminosity GRBs (a special family of long GRBs), which are believed to arise from a shock breakout from the stellar surface (Kulkarni et al. 1998; Campana et al. 2006; Nakar & Sari 2012; Nakar 2015). For a shock breakout to explain the observed γ-rays in GRB 170817A, it should take place at a radius of 10^{11}–10^{12} cm with $\Gamma \sim 3$.

While the γ-rays gave the first hint for a significant mildly relativistic outflow, the radio and X-ray afterglow provided a very strong support for this picture. The radio signal, which seems to be the mildly relativistic part of the radio flare predicted by Nakar & Piran (2011), rises continuously, roughly as $t^{0.8}$, since the first detection on day 16 (Hallinan et al. 2017; Mooley et al. 2018b), and so does the X-ray signal (Pooley et al. 2018; Margutti et al. 2018; Ruan et al. 2018). This moderate continuous increase is inconsistent with any type of off-axis emission (i.e., emission from material that moves with a Lorentz factor Γ at an angle larger than $1/\Gamma$ with respect to the observer). Instead, it requires a mildly relativistic blast wave with $\Gamma \sim$ 2–5 that radiates on-axis (Nakar & Piran 2018). Namely, the blast wave propagates into the interstellar medium (ISM) at a direction within an angle of $1/\Gamma$ with respect to the line of sight. The continuous rise in the radio implies that between day 10 and day 100 the energy in the region that radiates on-axis increased by about a factor of 10. The additional energy can be produced by a slower inner matter that is moving behind the blast wave and is catching up as it slows down or by matter moving on a slightly larger viewing angle that decelerates and comes into the line of sight (i.e., an angle $<1/\Gamma$; Nakar & Piran 2018). All these properties of the emitting blast wave fit very well the outcome of the interaction of the mildly relativistic cocoon (with either a choked or a successful jet) with the circum-merger ISM (Gottlieb et al. 2018b; Lazzati et al. 2018; Margutti et al. 2018).

The first goal of this paper is to find out whether a single model can explain all the electromagnetic observations, starting with the prompt gamma rays, through the UV/optical/IR macronova and up to the radio and X-ray afterglow. The second goal is to find out what future observations are needed to distinguish between different models that currently fit the data, and specifically whether there is a successful jet in GW170817 or not. For that we carry out a series of numerical hydrodynamic simulations with post-processing radiation calculations, which are the first to encompass the entire

evolution and emission, from the prompt γ-rays to the afterglow. A general description of the simulations is given in Section 2. In order to streamline the structure of the paper, the exact details of the simulations are discussed in the Appendix. We discuss the resulting light curves of the γ-rays, the UV/optical/IR macronova, and the radio afterglow in Section 3. In Section 4 we explore the differences in the predicted radio light curve, image, and polarization between a choked and a successful jet and discuss how future observations may distinguish between these two scenarios. We summarize our results and conclude in Section 5.

2. Methods

We have carried out a set of relativistic hydrodynamic simulations (see the Appendix for details) of the post-merger outflow starting at the jet launching; following its propagation through the subrelativistic ejecta and the cocoon shock breakout, where the γ-rays are produced; continuing to the homologous phase, during which the UV/optical/IR macronova is emitted; and ending in the interaction of the outflow with the circum-merger ISM that gives rise to the radio and the X-rays. We used the public code PLUTO (Mignone et al. 2007), with an HLL Riemann solver and a third-order Runge–Kutta time stepping.

The numerical simulations were done in two steps, spanning together over about 10 orders of magnitude in length scale, both for the hydrodynamics and for the radiation. The hydrodynamics begins on a scale of 10^8 cm, where we inject the jet, and it ends at about 10^{18} cm, the location of the blast wave 1000 days (as measured in the observer frame) after the event.

In each one of the relevant stages we post-process the hydrodynamic results and calculate the emission (see the Appendix for details). The prompt γ-ray emission upon the cocoon shock breakout takes place at a radius of $\sim 10^{11}$ cm, where the emitting region width is about 10^9 cm. The macronova signal is produced at 10^{15}–10^{16} cm, and the subsequent afterglow at 10^{16}–10^{18} cm. As initial conditions we take the subrelativistic ejecta that was ejected by the merger. The ejecta contained two components, a massive and slow component (0.05–0.1 $M_\odot$ at $0.1c$–$0.3c$), which is inferred from the UV/optical/IR emission, and a fast low-mass tail that is necessary, in our model, for the breakout to take place at a large enough radius to produce the observed γ-rays. This fast tail is not observed directly, but its existence was predicted as an outcome of the shock that formed during the first collision between the two neutron stars (Kyutoku et al. 2014), and it was found in early merger simulations (although with marginal resolution; Hotokezaka et al. 2013), where $\sim 10^{-6}$–$10^{-7} M_\odot$ has a velocity of $0.7c$–$0.8c$. Kiuchi et al. (2017) performed recently the highest-resolution merger simulations ever and confirmed the existence of this fast component. We have neglected the acceleration of the ejecta due to the radioactive heating, as the effect is insignificant compared to the already large velocity of the ejecta (Rosswog et al. 2014).

3. Results

In the various simulations we varied the jet and ejecta properties. We focused on relatively wide jets with opening angles of ∼0.5–0.7 rad. Such jets are uncollimated and are fully choked in the ejecta, dumping all their energy into the mildly
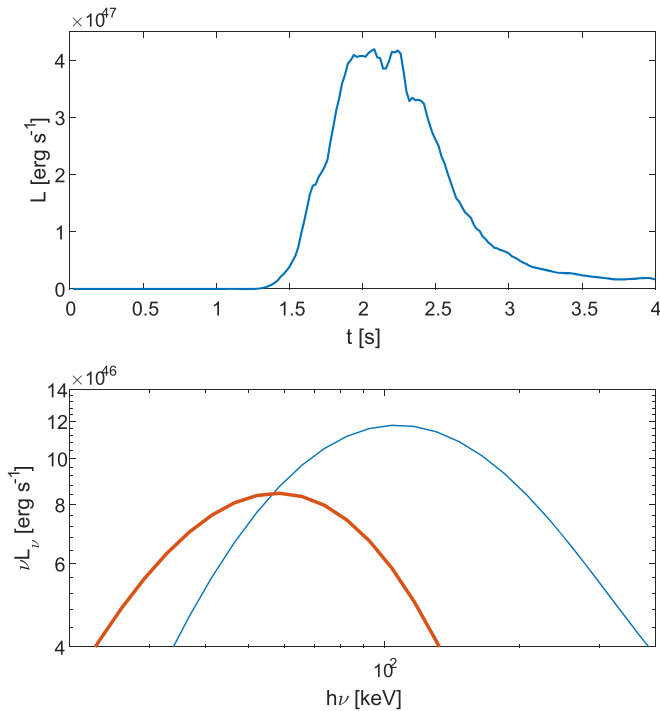
Figure 1. The γ-ray light curve (top panel) and spectrum (bottom panel) during the shock breakout from the uncollimated choked jet simulation describe in the Appendix. The spectrum is divided into the emission during the peak (blue line) and that during the tail (red line). The jet opening angle is 0.7 rad, and it is fully choked long before the shock driven by the cocoon breaks out of the ejecta fast tail. The observer is at an angle of 0.6 rad. The γ-ray signal shows the main properties of GRB 170817A (Goldstein et al. 2017). It starts rising about 1.5 s after the merger, having a peak that lasts about 0.5 s, followed by a longer decay that lasts an additional second. The peak luminosity is comparable to that of GRB 170817A to within an order of magnitude (about a factor of 3 brighter). The spectrum shows a hard-to-soft evolution where the peak of νF_ν is $E_p \approx 110$ keV during the initial pulse (integrated up to 2.3 s) and $E_p \approx 55$ keV during the tail (after 2.3 s). This should be compared to GRB 170817A, where in the initial pulse $E_p = 185 \pm 62$ keV and the tail's spectrum is consistent with a blackbody with $T \approx 10$ keV, where $E_p \approx 40$ keV.

relativistic cocoon. Only these jets can accelerate enough ejecta material to affect the early optical emission. Among those simulations, we looked for those that fit the entire set of observations, finding several. An example of the emission from such a simulation and a comparison to the observations are shown in Figures 1–3. The jet in this simulation has a luminosity of 2.6×10^{51} erg s^{-1} and an opening angle of 0.7 rad, and it is launched for 1 s starting 0.8 s after the merger. The observer is set at an angle of 0.6 rad with respect to the jet symmetry axis. In Figure 3 we show the afterglow for two different ISM densities; both fit current observations, but each has a different future prediction.

We also run two simulations of a narrow powerful jet with an initial opening angle of $10^{\rm o}$ and a luminosity of 6.7×10^{50} erg s^{-1}. In both simulations the jet and ejecta parameters are the same, and the only difference is the duration over which the jet is launched. In one simulation the jet is launched for a duration that is long enough that it successfully breaks out of the ejecta and presumably produces an sGRB that can be observed along its axis. This successful jet with its cocoon, which is sometimes called the "structured jet," is scenario E in Figure 2 of Mooley et al. (2018b), and it is similar to the one considered by Lazzati et al. (2018) and Margutti et al. (2018). In the second simulation the jet is launched for a
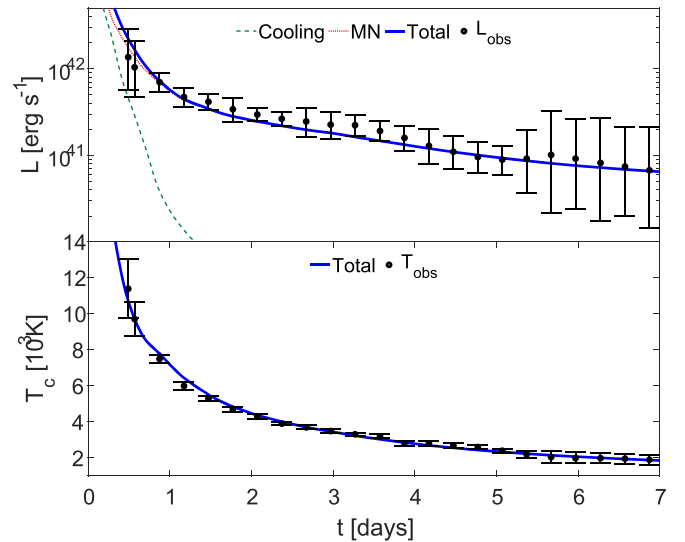

Figure 2. Optical light curve (top panel) and color temperature (bottom panel) from an uncollimated choked jet simulation (the same simulation and same observing angle as in Figure 1); see the Appendix for details. The data are taken from Kasliwal et al. (2017). Here we show the fit for a two-component ejecta, where the opacity of slow-moving material ($<0.1c$; mostly ejected along the equator) is 5 cm^2 g^{-1}, corresponding to a lanthanides-rich material, while that of fast-moving material is 0.8 cm^2 g^{-1}, consistent with the expectation for a lanthanides-poor material. A fit with a similar quality is obtained for a single lanthanides-poor component outflow with a constant opacity of 0.8 cm^2 g^{-1}. The contributions of the two power sources are shown: the cocoon cooling emission (dashed line) and the radioactive macronova (dotted line). The cocoon macronova emission is significant during the first day, after which the ejecta macronova dominates the emission.

short duration and is choked before breaking out of the ejecta. In both cases the cocoon does not affect the UV/optical emission on a timescale of half a day, but we show that the shock breakout of the successful jet can potentially generate the γ-ray signal (Figure 4). In both simulations there are afterglow parameters (ISM density and microphysics) for which the observed radio and X-ray emission is produced as shown in Figure 3.

4. Was There a Relativistic Jet in GW170817?

A relativistic jet is necessary to produce an sGRB. Therefore, the question whether a relativistic jet can successfully break out of a neutron star merger ejecta and in particular whether a jet broke out in this event is interesting. In GW170817 we consider the option of a successful jet as possible but less likely. First, it does not explain the early optical light. Second, and more importantly, to explain the observed radio emission, either the jet should be much weaker than the cocoon, so that its contribution is unimportant, or it should be so powerful that its contribution begins only at very late time, at least months after the merger. Without fine-tuning, the jet is not expected to have much less energy than the cocoon (Nakar & Piran 2017), while a very powerful jet produces a very luminous sGRB, and these are known to be extremely rare (Nakar 2007; Wanderman & Piran 2015). However, this is only circumstantial evidence.

Unfortunately, a weak successful jet does not contribute to the observed emission, and therefore we may never know whether it existed or not. A powerful jet, however, might be detectable. If it is powerful enough, it may be detectable while being still off-axis. In that case the radio light curve should rise sharply and then decline as a power law, after a short plateau.
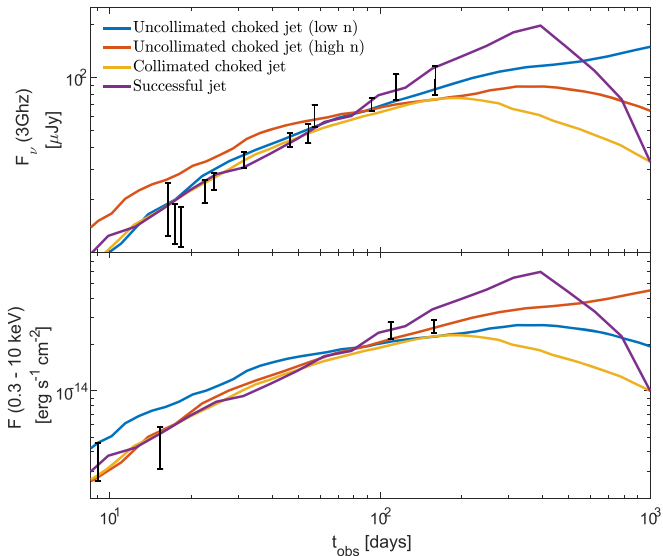
Figure 3. Afterglow emission compared with the radio and X-ray data (Hallinan et al. 2017; Troja et al. 2017; Margutti et al. 2018; Mooley et al. 2018b). Shown are four simulations, two uncollimated, both with a choked jet, and two collimated, one with a choked jet and one with a successful jet. In all simulations the observer is at 0.6 rad (see the Appendix). Both uncollimated choked jet simulations have the same outflow as in Figures 1 and 2. The difference is that one has a high ISM density and a low magnetic field ($n = 10^{-2}$ cm^{-3}, $\epsilon_B = 7 \times 10^{-5}$) while the other has a lower density and a higher magnetic field ($n = 2 \times 10^{-4}$ cm^{-3}, $\epsilon_B = 5 \times 10^{-3}$). The collimated choked jet afterglow simulation has $n = 3 \times 10^{-3}$ cm^{-3}, $\epsilon_B = 3 \times 10^{-3}$, and the successful jet simulation has $n = 10^{-2}$ cm^{-3}, $\epsilon_B = 5 \times 10^{-5}$. In all simulations $\epsilon_e = 0.1$ and $p = 2.17$. All models fit the observations very well, and in all of them the cocoon dominates the emission during most (if not all) of the available observations. The models start to deviate only after about 100 days. In the collimated cases (both choked and successful) the emission near the peak contains a significant contribution from material along the jet axis (in the successful case it is the jet), and following the peak there is a fast decline. The afterglows of uncollimated choked jets also reach a peak, but the following decline is typically shallower than the collimated jets. We note that the jet in the successful case is extremely energetic, with an isotropic equivalent luminosity of 4.4×10^{52} erg s^{-1}, which is unusually high for sGRBs. This is the main reason that its contribution starts so late.

This unique prediction of the jet signature is the easiest to identify. A less powerful jet may contribute to the radio light curve, but its contribution may not be easily identified (see, e.g., Figure 3 and Lazzati et al. 2018; Margutti et al. 2018), since a continuous rise to a peak followed by a decay can arise either from a successful or from a choked jet (see Figure 3 and Nakar & Piran 2018).

Additional information, especially in the radio near the time that the afterglow flux peaks, may provide the key to resolve this question. First, the radio image of the source is expected to be resolved soon. Figure 5 shows the images of a choked and a successful jet simulation. It shows that when there is a successful jet, the image becomes more symmetric and its centroid moves significantly (on a scale comparable to the image size), as the emission from the jet becomes more prominent. The jet dominates the emission once the light curve peaks and then the motion of the image centroid stops. This evolution is generic and is expected to be seen in all the cases in which a successful jet dominates the emission near the peak. The image of a choked jet is less predictive, as it depends on the details of the cocoon structure and varies between different simulations we carried out. However, its evolution is typically different from that of a successful jet. Generally, we found that it is much less symmetric near the peak of the light curve, and
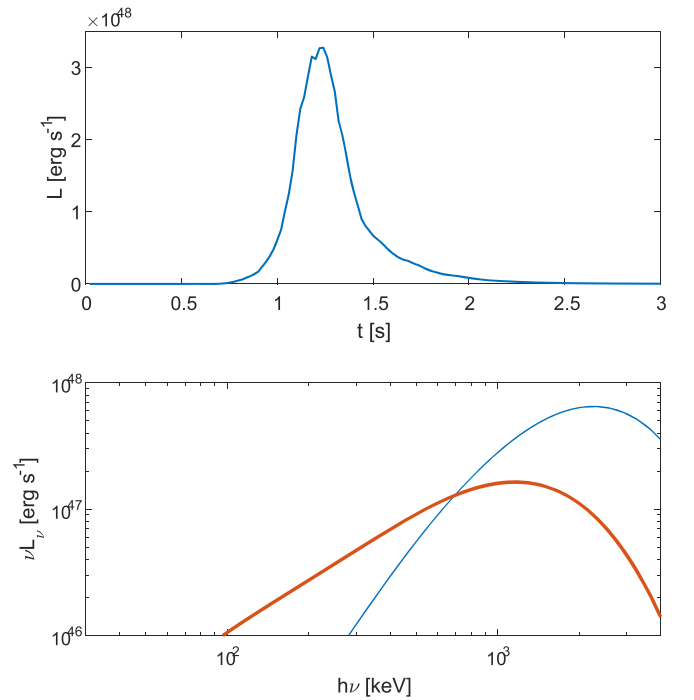

Figure 4. Shock breakout γ-ray light curve (top panel) and spectrum (bottom panel) from the successful jet simulation. The blue thin line is the spectrum during the peak, while the red thick line is the spectrum during the tail.

its centroid tends to move more slowly before the peak, than the image of a successful jet.

Linear polarization may provide an additional valuable clue (Ghisellini & Lazzati 1999; Sari 1999; Rossi et al. 2004; Granot & Taylor 2005; Gill & Granot 2018). The level of polarization depends on the geometry of the image and on the structure of the magnetic field. Therefore, the exact level of polarization at a given time will not give a definite answer; however, the time evolution differs significantly between a choked and a successful jet. A maximal polarization is seen when the source is moving at an angle of $1/\Gamma$ with respect to the line of sight (Sari 1999). Thus, if there is a dominant jet, then the polarization is expected to rise significantly as the jet becomes more dominant, reaching a peak in the polarization near or slightly after the peak of the light curve. After the peak, as the flux starts its decay, also the polarization level starts to drop. In contrast, the polarization of a choked jet is not expected to show significant evolution before and near the peak of the light curve. To conclude, while there may be uncertainty in interpreting any one piece of the information carried by the afterglow light, when added altogether we have a powerful tool at hand to resolve the structure of the outflow.

5. Conclusions

In summary, we have shown that the entire set of electromagnetic observations that followed GW170817 can be explained by the different phases in the evolution of a mildly relativistic cocoon, formed during the propagation of a relativistic jet through the subrelativistic ejecta. While the formation and evolution of the cocoon, as well as its importance for a signal observed away from the cone of the relativistic jet, were predicted before GW170817 (Lazzati et al. 2017a; Nakar & Piran 2017; Gottlieb et al. 2018a), here we show that it is much more important than what was thought
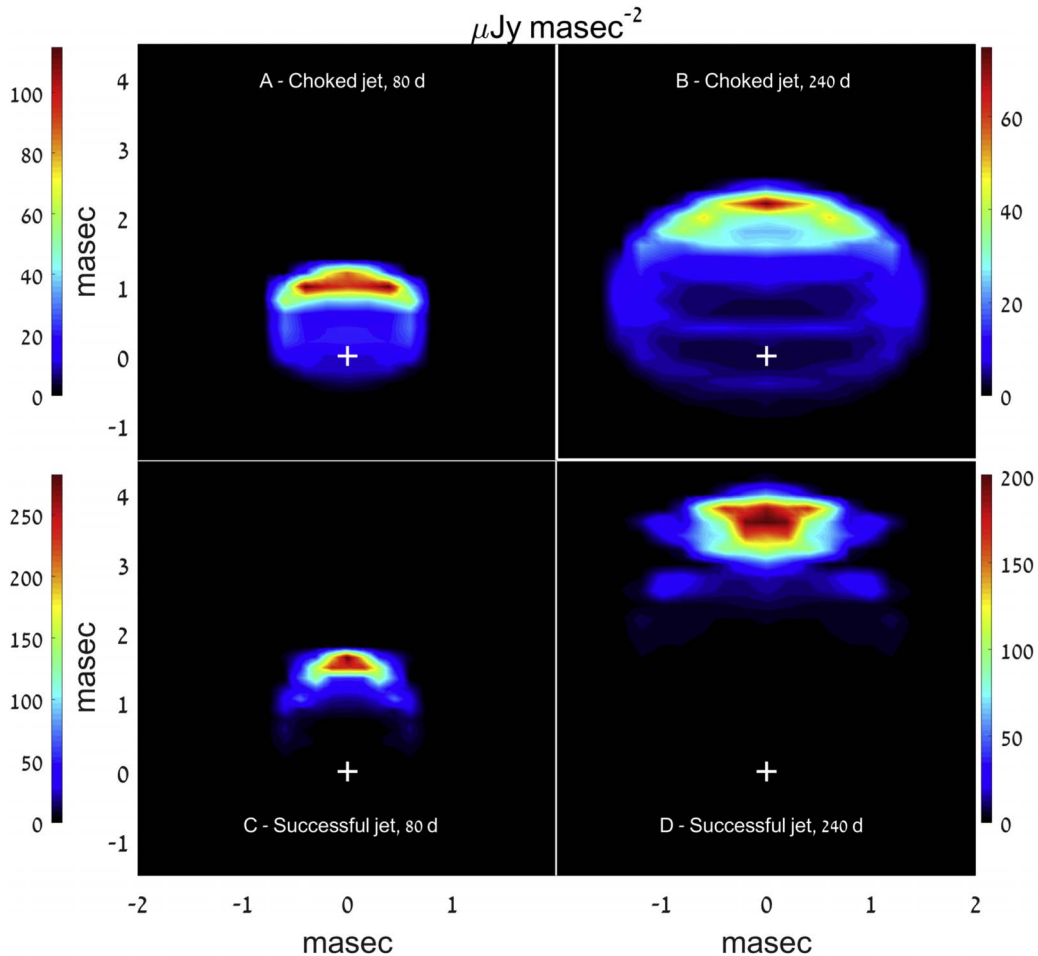
Figure 5. Radio images at 3 GHz for two of the simulations presented in Figure 3, the uncollimated choked jet with high density and the successful jet. The images are taken on day 80 (panels (a) and (c)) and day 240 (panels (b) and (d)), where the light curves of both afterglows peak. The plus signs at [0, 0] mark the line of sight. Both models show a roughly linear growth of the image size with time, to a size that should be resolved by the very long baseline interferometry (VLBI). By day 80 the jet is already the main contributor in the successful jet model, whereas the wider cocoon leads to a bigger image in case of a choked jet. By day 240 both shapes remain similar but have grown bigger over time, with the successful jet showing a more symmetric image with a centroid that is at a larger offset compared to the image on day 80. This is a general feature of successful jet images near the peak of the radio light curve, when the peak is dominated by the jet emission. We note that the image of the choked jet in this example is not general, and in other simulations (that fit the radio light curve) we see different image structures. The common property of most choked jet images is that they are asymmetric, with one axis of the image being longer than the other.

before. A clear prediction of this model is that future neutron star mergers will also show the signature of this mildly relativistic outflow.

The current[5] observations of GW170817 can be explained by a cocoon arising either from a choked jet or from a successful one, where in the latter case the jet may significantly contribute to the emission at late times.[6] While we favor the former, both are viable, and GW170817 may or may not have produced an sGRB. Therefore, GW170817 is not yet a conclusive evidence for the sGRB–NS merger connection. Nevertheless, it is certainly supporting this connection since it demonstrates that NS mergers most likely generate relativistic

jets, even if in this specific event the jet was choked. This is especially true given that the duration distribution of sGRBs shows evidence for a large number of failed sGRBs where the jet is choked (Moharana & Piran 2017).

---

[5] 2018 March.

[6] At the time that the paper was submitted various models could explain the observations. During the refereeing process, additional observations have shown a light curve that peaked around 150 days, which was followed by a decline roughly as t^{-2} and VLBI images that have shown a superluminal motion (Mooley et al. 2018a). As shown in Figure 5, out of the models discussed here only a narrow successful jet with very high isotropic equivalent energy is compatible with those observations (Mooley et al. 2018a). While a choked jet seems to be incompatible with GW1708178, the work we present here shows various models that may very well be relevant in future observations of compact binary mergers.

Appendix
Numerical Simulations

We carry out numerical relativistic hydro simulations of the jet–ejecta interaction and of the resulting outflow and its interaction with the surrounding matter. We then post-process the hydrodynamic results to calculate the observed emission. The hydrodynamics has four phases: (1) the jet–ejecta interaction and the formation of the cocoon; (2) the breakout of the cocoon (and the jet if it is not choked), and its expansion and acceleration until it reaches a homologous expansion; (3) a

phase of homologous expansion, during which the interaction with the external medium is unimportant; and (4) once enough ISM material is collected, the slowing down of the ejecta due to the strong blast wave it drives into the surrounding ISM. The hydro simulations are carried out in two steps. In step 1 we calculate the jet propagation within the ejecta and the cocoon breakout and expansion. This step ends when the cocoon material reaches a homologous expansion. During the homologous expansion phase, each element moves ballistically and cools adiabatically, and therefore we do not need to simulate this phase. We simply propagate the results from the end of phase I up to a radius that is smaller by about an order of magnitude than the radius at which the radio emission starts being significant. Then, we start step 2 of the simulation, which calculates the interaction of the outflow with the surrounding ISM.

We used the public code PLUTO (Mignone et al. 2007), with an HLL Riemann solver and a third-order Runge–Kutta time stepping. Throughout the simulations we apply an equation of state with a constant adiabatic index of 4/3, as appropriate for a radiation-dominated and relativistic gas. We neglect gravity, as the gravitational dynamical times are longer than the typical interaction timescales at all phases of the simulations.

The hydro simulation begins at the time of the merger, that is, $t = 0$, with a radially expanding cold ejecta (core and tail). After a fraction of a second, a relativistic jet is launched into the ejecta. The interaction of this jet with the ejecta forms a hot cocoon that eventually breaks out of the ejecta (with a jet in the successful case) at $r_{\rm bo}$. We let the relativistic outflow reach $(5–10)r_{\rm bo}$ before terminating the simulation at 1.2×10^{12} cm. We then stop the simulation and propagate the matter ballistically to a radius of $\sim 10^{16}$ cm, where we start it again to calculate the interaction with an external constant-density medium.

Following the hydro simulations, we post-process the data and calculate the observed radiation: the γ-rays during the shock breakout phase, the macronova's UV/optical/IR emission during the homologous expansion phase, and the radio and X-rays during the final stage of interaction with the ISM.

We carried out several simulations of uncollimated choked jets where we varied various parameters, such as the exact ejecta mass and velocity profile, the maximal ejecta velocity, and the jet luminosity and duration. We found several models where the resulting signals resemble the electromagnetic counterparts of GW170817. Here we describe one such simulation.

Simulations of collimated jets are much more demanding computationally (see below). We carried out, therefore, only two simulations, one of a successful jet and one of a choked jet. We found afterglow parameters for which the radio and X-rays from these simulations provide a good fit to the data (see Figure 3). We calculated the γ-ray signal from the simulation of the successful jet, and it is brighter and harder than GRB 170817A by about an order of magnitude (see Figure 4), but we expect that there are other parameters for which the shock breakout of a cocoon driven by a successful jet produces a γ-ray signal that is consistent with GRB 170817A.

A.1. Hydrodynamic Simulations—Uncollimated Choked Jet

We describe, first, the hydrodynamic simulation of the choked jet, whose results are shown in Figures 1–3. We use 2D

simulations for all the phases. This is justified since this jet is launched with a wide opening angle, and therefore it is uncollimated. When the jet is wide enough, mass accumulates ahead of its head, forming a "plug" that does not have enough time to spill sideways. Unlike narrow jets, for which the plug is artificial and arises as a result of the axial symmetry (the matter has time to spill sideways when the jet wiggles in the 3D simulations; see Section A.2 and Gottlieb et al. 2018a), the plug is physical in wide jets. To confirm this intuitive understanding, we carried out 2D and 3D simulations with the same physical setup and found, for wide jets, similar structures.

As initial conditions for part 1 we set the ejecta to be present from the base of the grid at $r_{\rm min} = 4 \times 10^8$ cm up to $r_{\rm max} = 5.2 \times 10^9$ cm. The ejecta is composed of two components, a massive and slow component, which we describe as the core, and a low-mass fast component, which we denote as the tail. The core extends from $r_{\rm min}$ to $r_{\rm max}/4$, and the fast tail from $r_{\rm max}/4$ to $r_{\rm max}$. The core ejecta's density profile is

$$\rho_c(r, \theta) = \rho_0 r^{-2}\left(\frac{1}{4} + \sin^3\theta\right), \tag{1}$$

where ρ_0 is chosen for a total core ejecta mass $M_c = 0.1\,M_\odot$. Namely, the angular dependence is such that 3/4 of the ejecta mass is near the equator at 1.0 rad $< \theta < \pi - 1.0$ rad, where θ is the angle with respect to the jet axis. The velocity profile of the core is

$$v_c(r) = v_{c,\rm max}\frac{r}{r_c}, \tag{2}$$

where $v_{c,\rm max} = 0.2c$ is the core's maximal velocity. The normalization of the fast-tail density is chosen so that its total mass is $M_t = 5 \times 10^{-3}\,M_\odot$, with a steep power law $\rho \propto v^{-14}$ and maximal velocity $0.7c$. With this velocity profile only $10^{-8}\,M_\odot$ are moving at $v \geqslant 0.6c$.

The jet is injected into the ejecta with a delay of 0.8 s for a total working time of 1 s and a total luminosity of $L_j = 2.6 \times 10^{51}$ erg s^{-1}. The jet is injected with a specific enthalpy of 20 at an opening angle of 0.7 rad from a nozzle at the base of the grid with a size of 10^8 cm.

We use a 2D cylindrical symmetric grid where the symmetry axis is z. For the grid of the first part of the simulation (from merger until the homologous phase) we use three patches along the x-axis; the innermost one in the x-axis resolves the jet's nozzle with 20 uniform cells from $x = 0$ to $x = 2 \times 10^8$ cm, the next patch stretches logarithmically from $x = 2 \times 10^8$ cm to $x = 2 \times 10^{10}$ cm with 800 cells, and the last patch has 1200 uniform cells to $x = 1.2 \times 10^{12}$ cm. In the z-axis we employ two uniform patches, one from $z_{\rm min} = 4.5 \times 10^8$ cm to $z = 2 \times 10^{10}$ cm with 800 cells, and the second to $z = 1.2 \times 10^{12}$ cm with 1200 cells. In total the grid contains 2020×2000 cells.

For the second part of the simulation we propagate the last snapshot of the first simulation ballistically to a radius of $\sim 10^{16}$ cm, where we let the relativistic outflow interact with the ISM. We verify that taking a smaller initial radius for this part does not affect the radio and X-ray light curve at the times of the observations. The simulation can be scaled, so a single simulation can be used to calculate the hydrodynamic evolution in different ISM densities over a different range of radii (Granot 2012). We present results for two such scalings, each with a different ISM number density and different radii R_1 and R_2 for the patches of the grid. For the high ISM number

density we use $n = 5 \times 10^{-2}$ cm^{-3} with $R_1 = 7 \times 10^{15}$ cm and $R_2 = 4 \times 10^{17}$ cm. In the second simulation we use $n = 5 \times 10^{-4}$ cm^{-3} with $R_1 = 3.2 \times 10^{16}$ cm and $R_2 = 1.8 \times 10^{18}$ cm. The grids are divided into two patches on each axis, the first of which is uniform with 500 cells on each axis, from 0 to R_1 in the x-axis and from $z_{\min}$ to R_1 in the z-axis. This patch contains the entire grid of the final snapshot of part 1 (propagated ballistically). The outer patches are identical, with 4000 cells in each axis, which are distributed logarithmically between R_1 and R_2. In total the grid has 4500×4500 cells.

A.2. Hydrodynamic Simulation—Collimated Successful and Choked Jets

We turn now to describe the details of the hydrodynamic simulation of the collimated jets. Here, the initial phase of the jet propagation within the ejecta core must be carried out using high-resolution 3D simulations (Gottlieb et al. 2018a). Note that 3D simulations are essential here, as they allow the jet to wiggle and avoid a heavy plug ahead of it. Such a plug is found in 2D simulations. We find that in 3D only a light plug ($\sim 10^{-8} M_\odot$ for a jet with opening angle of 8°) remains. 2D simulations, on the other hand, show a heavier plug that has a considerable effect on the jet's propagation. This phenomenon is caused by the fact that both the material and the jet are locked on the same plane. Therefore, we conclude that a plug on top of a collimated jet is artificial. This phase is very demanding computationally, and therefore we carry out only two simulations. After the jet crosses the ejecta core and expands into the fast tail, it is not collimated anymore and the evolution in 2D and 3D is expected be similar. We therefore take the result of the 3D simulation upon breakout of the jet from the core and map it to 2D by averaging over the azimuthal angle. We then continue the simulation in 2D (Lazzati et al. 2017b).

We run two identical simulations except for a single difference, the jet launching time, so that in one simulation the jet is choked while in the other it is successful. In both simulations at $t = 0$ a cold ejecta with $M_c = 0.05 M_\odot$ and $v_{c,\max} = 0.2c$ is present from $r_{\min} = 1.3 \times 10^8$ cm up to $r_{\max} = 3r_{\min}$ with a radial density profile $\rho \propto r^{-3.5}$. At $t = 0.72$ s a narrow jet with an opening angle of 10° is injected into the system. The jet has an initial velocity of $0.7c$, a specific enthalpy of 20, and a total luminosity of 6.7×10^{50} erg s^{-1}. In one simulation the jet is launched continuously for 1 s, and it breaks out of the ejecta successfully. In the second simulation the jet is launched for 0.4 s, and it is choked when its head is crossing most of the core ejecta. We stop the 3D simulations at $t = 1.4$ s, which is the time at which the successful jet breaks out of the core ejecta and the choked jet is fully choked, and convert the 3D grid to 2D, while adding a homologous fast-tail ejecta with a total mass $M_t = 2 \times 10^{-3} M_\odot$, a density profile $\rho \propto r^{-10}$, and a velocity range of $0.2c$–$0.8c$. Note that the density profile of the fast tail is such that most of the tail is moving at a velocity closer to $0.2c$. Only a tiny fraction $\sim 10^{-6} M_\odot$ is moving at $v > 0.7c$. The grids of the choked and successful jet scenarios are identical.

The grid of the 3D simulation is divided into two patches in each axis, where z is the jet symmetry axis. The inner patches are distributed uniformly in x and y (100 cells each) and z (400 cells) axes, extending to $\pm 3 \times 10^8$ cm and 6×10^9 cm, respectively. The z-axis begins at $z_{\min} = 1.3 \times 10^8$ cm. The

second patches are logarithmic, with 480 and 600 cells up to $\pm 9 \times 10^{10}$ cm in x and y and 1.2×10^{11} in z. In total the 3D simulation contains $600 \times 600 \times 1000$ cells.

After the 3D simulation ends, its grid is mapped to a 2D grid with the exact same cell sizes in x and z, and another patch is added to the grid in each axis, stretching to 1.2×10^{12} cm and 1.5×10^{12} cm with 1200 and 1500 uniform cells in x and z axes, respectively. In total the 2D simulation contains 1490×2560 cells and lasts 50 s.

For part 2 we take the last snapshot of part 1 as the initial conditions and repeat the same procedure and cell distribution of the uncollimated simulation. Namely, we use different scalings for the successful and choked jet cases. For the former we use $n = 5 \times 10^{-2}$ cm^{-3}, $R_1 = 1.3 \times 10^{16}$ cm, and $R_2 = 6.8 \times 10^{18}$ cm. For the latter we use $n = 2 \times 10^{-2}$ cm^{-3}, $R_1 = 10^{16}$ cm, and $R_2 = 5.7 \times 10^{18}$ cm.

A.3. γ-ray Emission

The γ-ray emission following the shock breakout is calculated in the following way. First, for each angle θ we determine the time $t_{\rm bo}(\theta)$ and radius $r_{\rm bo}(\theta)$ at which the shock breaks out from the ejecta at this angle. The luminosity is then calculated by finding the photons that diffused to the photosphere during the time that passed since the shock crossing, approximating the diffusion as being radial. Specifically, at each lab frame time $t > t_{\rm bo}$ and angle θ we find the location r_0 from which the photons diffuse to the observer. Namely, we find the location where the diffusion time to the photospheric radius, $r_{\rm ph}$ ($\tau(r_{\rm ph}) = 1$), equals the time that passed since breakout:

$$r_0 - r_{\rm ph} = \frac{t - t_{\rm bo}}{\Gamma(r_0)^2} \frac{c}{\tau(r_0)}, \qquad (3)$$

where $\Gamma(r_0)$ is the Lorentz factor of the emitting region. The energy, as measured in the fluid rest frame, released between t_1 and t_2 from a solid-angle element $d\Omega$ is the total internal energy of the emitting region during this period:

$$dE'(t_1, t_2, \theta) = \int_{r_0(t_1)}^{r_0(t_2)} 4p(r)\Gamma(r)r^2 dr d\Omega. \qquad (4)$$

At the first time step we take $r_0(t_1) = \infty$. To find the contribution to the observed energy, we boost dE' from the rest frame of the photosphere to the observer frame and take into account the light-travel time from $r_{\rm ph}(\theta)$ to the observer. The total observed luminosity is found by integrating on all times at $t > t_{\rm bo}$ over the solid angle.

The spectrum of the emitted radiation at each time step from each angle is approximated by a Wien spectrum, where the rest-frame temperature is calculated using the procedure described in Gottlieb et al. (2018b). For each fluid element that releases the energy within a given time step we find temperature, T, for which the number density of photons that are generated within this fluid element during available time is $e/3kT$. We approximate this number by using the pressure and the density of the element at the time at which its energy is released, and we solve Equation (5) of Gottlieb et al. (2018b) taking the available time as the maximum between the time that passed since the element was shocked and the time it takes the shock to cross the breakout layer (where $\tau = c/v_{\rm sh}$). If the temperature is higher than 50 keV, then pairs are created,

preventing the release of photons until the temperature drops to ≈ 50 keV, and in such a case we set the temperature of the emitted radiation to 50 keV.

This calculation is very rough and can be trusted to within a factor of a few both in the light curve and in the spectrum. The breakout itself takes place from the region where $\tau \approx 1$. On this scale the hydrodynamic equations that the code solves are not applicable, and therefore for the this regime we resort to an analytic approximation that is based on Nakar & Sari (2012). An uncertain aspect, which we do not follow accurately, is the creation and annihilation of pairs. Instead, we approximate the point where pairs annihilate and their opacity becomes insignificant to the time where the rest-frame temperature drops to 50 keV (see justification in Nakar & Sari 2012). Another quantity that we approximate is the rest-frame temperature. This is based on a quasi-steady-state approximation as discussed in Budnik et al. (2010) and Nakar & Sari (2012). Nevertheless, while the calculation is accurate only to within an order of magnitude, we expect that it does provide a good description of the general light curve and spectral evolution.

A.4. UV/Optical/IR Emission

We are interested in fitting the bolometric luminosity and temperature evolution of the UV/optical/IR counterpart of GW170817. We restrict the fit to the first week, after which both the luminosity and the temperature are not well constrained. For the hydrodynamic evolution we use the final snapshot of part 1 of the choked jet hydrodynamical simulation, taken at time t_f. The homologous expansion after that time enables us to calculate the evolution of each fluid element and the adiabatic cooling of the radiation trapped in the fluid at any time $t > t_f$.

We estimate the opacity of the ejecta using two components, a low-opacity component that corresponds to lanthanides-poor material and a high-opacity component that corresponds to lanthanides-rich material. This is motivated both by theoretical considerations that suggest that the ejecta at high latitudes is lanthanides-free while the outflow at low latitudes is lanthanides-rich (e.g., Perego et al. 2014; Kasen et al. 2015) and, more importantly, by the spectral evolution of the UV/optical/IR counterpart of GW170817 (e.g., Evans et al. 2017; Smartt et al. 2017). We find a good fit to the data during the first week (Figure 2) using $\kappa = 0.8$ cm^2 g^{-1} for material moving at $v > 0.1c$ and $\kappa = 5$ cm^2 g^{-1} for material moving at $v < 0.1c$. This velocity criterion is applicable since the interaction with the jet accelerates the material at high latitudes to $v > 0.1c$. We also test whether a single-component model can fit the data (e.g., Smartt et al. 2017) and find that a good fit (at least to the luminosity and temperature) can be obtained with a single component where all the ejecta have $\kappa \approx 0.8$ cm^2 g^{-1}.

The emission is calculated assuming that the photons diffuse radially. For each angle θ, we calculate first the optical depth to infinity, $\tau(r, \theta)$. We determine the trapping radius $r_t(\theta)$ where $\tau(r_t(\theta)) = c/v$, above which photons diffuse freely to the observer, and the photosphere $r_{ph}(\theta)$ in which $\tau(\theta) = 1$.

The emission is powered by two sources: the diffusion of the internal energy (cooling emission), and the radioactive heating (macronova). For the cooling emission we find the rest-frame energy flux at $r_t(t, \theta)$, which has been trapped up until the current time t:

$$\Phi(t, \theta)_{\text{cool}} = 4p_t r_t(\theta)^2 v_t d\Omega \, , \quad (5)$$

where p_t and v_t are the pressure and velocity at $r_t(\theta)$.

We approximate the macronova luminosity as coming from the instantaneous heating rate at $r > r_t$:

$$\Phi(t, \theta)_{\text{MN}} = \int_{r_t(\theta)}^{\infty} \dot{\epsilon}\rho(r)\Gamma(r)r^2 dr d\Omega \, , \quad (6)$$

where ρ and Γ are the density and Lorentz factor of the emitting region, resepectively, and the radioactive heating rate per unit of mass is approximated as (e.g., Hotokezaka et al. 2016)

$$\dot{\epsilon} \approx \dot{\epsilon}_0(f_\gamma(t) + 0.5f_e(t))\left(\frac{t}{\text{day}}\right)^{-\alpha} \, , \quad (7)$$

where $\dot{\epsilon}_0 \sim 10^{10}$ erg g^{-1} s^{-1} and $\alpha \approx -1.1$ to -1.4. Here f_γ and f_e are the fractions of the energy in gamma rays and electrons that is deposited in the ejecta, respectively. As we are interested in the emission during the first week, we approximate $f_e = 1$ and $f_\gamma = 1 - e^{-\left(\frac{t_0}{t}\right)^2}$, where $t_0 \sim 1$ day is the typical gamma-ray escape time. For the fit presented in Figure 2 we use $\dot{\epsilon}_0 = 2 \times 10^{10}$ erg g^{-1} s^{-1}, $\alpha = 1.1$, and $t_0 = 0.7$ days.

Along each angle we approximate the emission at any time as being emitted isotropically at the photospheric radius, $r_{ph}(\theta)$, with a luminosity $\Phi(t, \theta)_{\text{cool}} + \Phi(t, \theta)_{\text{MN}}$ in the photosphere rest frame. We also approximate the emission as being in thermal equilibrium at the photosphere, so emitted spectrum is a blackbody with a rest-frame temperature that corresponds to the luminosity and $r_{ph}(\theta)$. Finally, similarly to A.3, we integrate and boost the luminosity and temperature to the observer's reference frame. The spectrum that we obtain from the integration is not a blackbody, and the temperature that we present is the color temperature.

A.5. Radio and X-Ray Afterglow Emission

We model the afterglow emission by the synchrotron radiation of relativistic electrons accelerated in the shocks formed between that cocoon and the ISM. We use the standard afterglow modeling that parameterizes the microphysics using a constant fraction of the internal energy that goes to electrons, ϵ_e, a constant fraction of the internal energy that goes to the magnetic field, ϵ_B, and a power-law distribution for the accelerated electrons with index p. Given the low density of the ISM, the radio and the X-ray bands are not affected by cooling or by absorption, and both bands are on a single power-law segment above the typical synchrotron and self-absorption frequencies and below the cooling frequency. Note that this assumption is clearly valid for the observed regions, as it agrees with the observed spectrum, but it might not be generally valid. Therefore, the emission from each fluid element is not affected by its history (i.e., cooling) or by the conditions in other fluid elements (i.e., absorption).

Using the microphysical parameterization and the pressure and density in each cell at each time step, we find the electron distribution and the magnetic field and calculate the rest-frame synchrotron emissivity using standard afterglow theory (e.g., Sari et al. 1998). Then, to find the observed luminosity at each observing angle, we integrate over equal arrival time surfaces taking the proper Lorentz boost from each element.

Since the radio and the X-rays are on the same spectral power-law index, $-(p-1)/2$, the observations set $p = 2.17$. We also set $\epsilon_e = 0.1$. The free parameters we have are external density, n, and ϵ_B. The values we use to fit the data in the various simulations (which are not unique) are given in Figure 3.

The calculation of the synchrotron emission requires the shock to be resolved. This demand is harder to achieve when the emitting region has a higher Lorentz factor since the width of the shocked region is $\sim R/\Gamma^2$. In this paper we calculated the emission seen by an observer at an angle of 0.6 rad, and the emission is always dominated by a region with a moderate $\Gamma < 4$. We verify that the emitting region is always resolved in our calculations, and we carried out a convergence test to verify that the light curve is not affected by the resolution we take. The images were calculated in a resolution of 0.1×0.1 mas^2. This is about an order of magnitude higher than the VLBI resolution. Also here we carried out a convergence test to verify that the image shape is not affected by the resolution.

ORCID iDs

Tsvi Piran ⓘ https://orcid.org/0000-0002-7964-5420
Mansi. M. Kasliwal ⓘ https://orcid.org/0000-0002-5619-4938

References

Arcavi, I. 2018, ApJL, 855, L23
Arcavi, I., Hosseinzadeh, G., Howell, D. A., et al. 2017, Natur, 551, 64
Bromberg, O., Tchekhovskoy, A., Gottlieb, O., Nakar, E., & Piran, T. 2018, MNRAS, 475, 2971
Buckley, D. A. H., Andreoni, I., Barway, S., et al. 2018, MNRAS, 474, L71
Budnik, R., Katz, B., Sagiv, A., & Waxman, E. 2010, ApJ, 725, 63
Campana, S., Mangano, V., Blustin, A. J., et al. 2006, Natur, 442, 1008
Coulter, D. A., Foley, R. J., Kilpatrick, C. D., et al. 2017, Sci, 358, 1556
Covino, S., Wiersema, K., Fan, Y. Z., et al. 2017, NatAs, 1, 791
Cowperthwaite, P. S., Berger, E., Villar, V. A., et al. 2017, ApJL, 848, L17
Díaz, M. C., Macri, L. M., Garcia Lambas, D., et al. 2017, ApJL, 848, L29
Drout, M. R., Piro, A. L., Shappee, B. J., et al. 2017, Sci, 358, 1570
Eichler, D., Livio, M., Piran, T., & Schramm, D. N. 1989, Natur, 340, 126
Evans, P. A., Cenko, S. B., Kennea, J. A., et al. 2017, Sci, 358, 1565
Ghisellini, G., & Lazzati, D. 1999, MNRAS, 309, L7
Gill, R., & Granot, J. 2018, MNRAS, 478, 4128
Goldstein, A., Veres, P., Burns, E., et al. 2017, ApJL, 848, L14
Gottlieb, O., Nakar, E., & Piran, T. 2018a, MNRAS, 473, 576
Gottlieb, O., Nakar, E., Piran, T., & Hotokezaka, K. 2018b, MNRAS, 479, 588
Granot, J. 2012, MNRAS, 421, 2610
Granot, J., Gill, R., Guetta, D., & De Colle, F. 2018, MNRAS, 481, 1597
Granot, J., & Taylor, G. B. 2005, ApJ, 625, 263
Haggard, D., Nynka, M., Ruan, J. J., et al. 2017, ApJL, 848, L25
Hallinan, G., Corsi, A., Mooley, K. P., et al. 2017, Sci, 358, 1579
Hotokezaka, K., Kiuchi, K., Kyutoku, K., et al. 2013, PhRvD, 87, 024001
Hotokezaka, K., Nissanke, S., Hallinan, G., et al. 2016, ApJ, 831, 190
Kasen, D., Fernández, R., & Metzger, B. D. 2015, MNRAS, 450, 1777
Kasen, D., Metzger, B., Barnes, J., Quataert, E., & Ramirez-Ruiz, E. 2017, Natur, 551, 80
Kasliwal, M. M., Nakar, E., Singer, L. P., et al. 2017, Sci, 358, 1559
Kilpatrick, C. D., Foley, R. J., Kasen, D., et al. 2017, Sci, 358, 1583
Kiuchi, K., Kawaguchi, K., Kyutoku, K., et al. 2017, PhRvD, 96, 084060
Kulkarni, S. R., Frail, D. A., Wieringa, M. H., et al. 1998, Natur, 395, 663
Kyutoku, K., Ioka, K., & Shibata, M. 2014, MNRAS, 437, L6
Lazzati, D., Deich, A., Morsony, B. J., & Workman, J. C. 2017a, MNRAS, 471, 1652
Lazzati, D., López-Cámara, D., Cantiello, M., et al. 2017b, ApJL, 848, L6
Lazzati, D., Perna, R., Morsony, B. J., et al. 2018, PhRvL, 120, 241103
Lyman, J. D., Lamb, G. P., Levan, A. J., et al. 2018, Natur, 2, 751
Margutti, R., Alexander, K. D., Xie, X., et al. 2018, ApJL, 856, L18
Margutti, R., Berger, E., Fong, W., et al. 2017, ApJL, 848, L20
McCully, C., Hiramatsu, D., Howell, D. A., et al. 2017, ApJL, 848, L32
Mignone, A., Bodo, G., Massaglia, S., et al. 2007, ApJS, 170, 228
Moharana, R., & Piran, T. 2017, MNRAS, 472, L55
Mooley, K. P., Deller, A. T., Gottlieb, O., et al. 2018a, Natur, 561, 355
Mooley, K. P., Nakar, E., Hotokezaka, K., et al. 2018b, Natur, 554, 207
Nakar, E. 2007, PhR, 442, 166
Nakar, E. 2015, ApJ, 807, 172
Nakar, E., & Piran, T. 2011, Natur, 478, 82
Nakar, E., & Piran, T. 2017, ApJ, 834, 28
Nakar, E., & Piran, T. 2018, MNRAS, 478, 407
Nakar, E., & Sari, R. 2012, ApJ, 747, 88
Nicholl, M., Berger, E., Kasen, D., et al. 2017, ApJL, 848, L18
Perego, A., Rosswog, S., Cabezón, R. M., et al. 2014, MNRAS, 443, 3134
Pian, E., D'Avanzo, P., Benetti, S., et al. 2017, Natur, 551, 67
Pooley, D., Kumar, P., & Wheeler, J. C. 2018, ApJL, 859, L23
Pozanenko, A. S., Barkov, M. V., Minaev, P. Y., et al. 2018, ApJL, 852, L30
Ramirez-Ruiz, E., Celotti, A., & Rees, M. J. 2002, MNRAS, 337, 1349
Rossi, E. M., Lazzati, D., Salmonson, J. D., & Ghisellini, G. 2004, MNRAS, 354, 86
Rosswog, S., Korobkin, O., Arcones, A., Thielemann, F.-K., & Piran, T. 2014, MNRAS, 439, 744
Ruan, J. J., Nynka, M., Haggard, D., Kalogera, V., & Evans, P. 2018, ApJL, 853, L4
Sari, R. 1999, ApJL, 524, L43
Sari, R., Piran, T., & Narayan, R. 1998, ApJL, 497, L17
Savchenko, V., Ferrigno, C., Kuulkers, E., et al. 2017, ApJL, 848, L15
Shappee, B. J., Simon, J. D., Drout, M. R., et al. 2017, Sci, 358, 1574
Smartt, S. J., Chen, T.-W., Jerkstrand, A., et al. 2017, Natur, 551, 75
Soares-Santos, M., Holz, D. E., Annis, J., et al. 2017, ApJL, 848, L16
Tanaka, M., Utsumi, Y., Mazzali, P. A., et al. 2017, PASJ, 69, 102
Tanvir, N. R., Levan, A. J., González-Fernández, C., et al. 2017, ApJL, 848, L27
Troja, E., Piro, L., van Eerten, H., et al. 2017, Natur, 551, 71
Utsumi, Y., Tanaka, M., Tominaga, N., et al. 2017, PASJ, 69, 101
Wanderman, D., & Piran, T. 2015, MNRAS, 448, 3026
Waxman, E., Ofek, E., Kushnir, D., & Gal-Yam, A. 2018, MNRAS, 481, 3423